Available online at www.sciencedirect.com

ScienceDirect

Procedia Structural Integrity 68 (2025) 66–76

Structural Integrity Procedia

www.elsevier.com/locate/procedia

European Conference on Fracture 2024

Shape memory-based lattice metamaterial: the octet truss cell

C. Corda[a], E. Armentani[a], C. Bertolin[b,*], C. Gao[b]

[a]*Department of Industrial Engineering, University of Naples Federico II, Naples, Italy*
[b]*Department of Mechanical and Industrial Engineering, NTNU, Trondheim, Norway*

Abstract

Lattice metamaterial attracted great attention in the last years due to their intelligent behaviour when subjected to external stimuli, which is also denoted as shape memory effect. This is the principle on how the 4D Additive Manufacturing is based on: it is possible to create complex geometry making the material "programmable" building up self-assembly structures. In this preliminary study, the octet lattice metamaterial has been selected to evaluate its performance by taking into account of shape memory effect investigating on its great properties in adaptability in shock absorption, negative Poisson's ratio, high stiffness and weight efficiency with previous studies conducted in literature; its structure as designed on the commercial software ABAQUS. Through the finite element analysis has been possible to perform the structure under uniaxial compression test studying its response under specific loads changing geometrical configurations -e.g., relative density, diameter of truss- to fully understand the mechanism of the octet lattice metamaterial. The preliminary results show clearly great potential offered by octet truss lattice metamaterial with shape memory effect in terms of shape and stress recovery and in terms of planned structure degradation which could be advantageously exploited in future for many industrial applications.

Keywords: Shape Memory Polymer; Octet Truss Cell; Metamaterial; 4D-printing.

* Corresponding author.
E-mail address: chiara.bertolin@ntnu.no

2452-3216
10.1016/j.prostr.2025.06.024

1. Introduction and state of art

Metamaterial with shape memory effect has received many interests and most studies focus on the actuating behaviour/programable deformation induced by shape memory effect. Latticed metamaterial is one of the top star in this field and offers extraordinary potential for industrial application. The shape-memory effect (SME) is the material's ability to change shape or properties over time when subjected to external stimuli such as temperature, moisture, light or other external factors. This effect is studies in the shape-memory polymers (SMPs), a class of smart polymers that, compared to other materials, have a much lower material cost and lower density which enable the material to be wider studies in their shape-memory performance being the change of their shape easily to reproduce. To make this type of metamaterial meet wider industrial need, the mechanical performance becomes more important. However, few studies have been performed yet. SMPs has stimulated great interest in different fields of application such as robotics, aerospace, biomechanics and textile for their stimuli-responsive properties, giving rise to the 4th dimension (i.e. the temporal one) of the additive manufacturing technologies called 4D printing. Differently from the 3D printing technologies, which enables the fabrication of complex lattice structure in a no-reconfigurable way; 4D printing leads the material to deform and to change its properties under external stimulus such as thermal stimulus (Yang et al. 2019) or UV lights exposure (Azzawi et al. 2018) demonstrating that the molecular structure of the polymer begins to degrade reducing the elasticity and the tensile strength. However, materials have been developed into complex meta-structures enhancing their mechanical properties while significantly lowering their density for accomplish with sustainable goals (Pihraji et al. 2020). This leads to make the properties dependent on geometry rather than on composition through the repeating of unit cells. Within the framework of geometry optimization, lattice structures can exhibit unusual properties by arranging or adjusting their unit cell structure. In particular, the octet truss lattice structure is a type of synthesized metamaterial first proposed by Fuller (1961) with a unit cell with 12 nodal connections forming a face centered cubic configuration. The octet is a stretching dominated structure and it offers great advantages in terms of weight efficiency, energy absorption, simplicity of fabrication for its design and high stiffness to mass ratio. By adjusting the strut thickness and node configuration, the octet's mechanical properties can be tuned to enhance shock absorption and deformation recovery. In particular, relative density dictates the deformation mode of the structure and it is defined as the ratio of the lattice density to the density of the base material. Deshpande et al. (2001) found a relation between the relative density and the geometrical parameters. Latture et al. (2015) suggested that the increase of the strut thickness enhances the structure's bending stiffness, especially in regions close to the nodal points, contrary, Chen et al. (2018) demonstrated that, at lower relative densities (0.22-0.23), the structure tend to exhibit shear-dominated failure, whereas at higher relative densities the structure leads to buckling-free compression, providing greater stability and load resistance. Ling et al. (2019) discovered that, by adjusting the relative density and pre-compression strain, an increase in the diameter of struts improves the octet truss' stress recoverability. The materials exhibited high shape recovery, but force recovery decreased as density dropped, especially in ultra-low density samples. Pirhaji et al. (2020) demonstrated that, thinner struts in octet trusses, lead to shear-mode deformation, while thicker struts result in buckling-free behavior, particularly at higher relative densities. Therefore, the goal of our study is to fill the knowledge gap. Particularly, the quasi-static compression has been investigated numerically the octet truss structure in terms of energy absorption ability of different relative density and high stiffness to mass ratio choosing a simple and effective design. In this paper we proposed an advanced model of the octet truss lattice structure to improve its mechanical performance under uniaxial compression test. Beside this introduction and state of the art (section 1), the methodological approach (section 2), through detailed simulations conducted using the ABAQUS software for finite element analysis (FEA) , has designed an hybrid geometry made up of the octet truss cell (O) and the body cubic (BC) to form the merged BC-O truss which can represent a good compromise between flexibility and mechanical stability. In this regard, the BC has been chosen for its simple structure and for its lightweight. In section 3 Results are presented and discussed. Finally in section 4 conclusions are stated

2. Materials and Methods

In this section, the principles of a representative volume element (RVE) have been used to model the BC-O truss model. Three BC-O lattice structures have been modeled by commercial software ABAQUS with 1x1x1 mm unit cells. The diagonal length L was set as 0.707mm with three different strut sections b/a=0.5, b/a=1, b/a=2 where a=0.1

mm is representing an axis of the ellipse keeping constant its value while b is the other axis and it changes varying the ratio (Figure 1). As showed in the Figure 2, The BC structure is inserted into the octet truss intersecting the lateral beams to the four internal nodes (P2,P3); the straight beams, instead, intersect the central nodes on the top and bottom surfaces (P1,P4).
The fundamental parameters are defined in the table 1 below:

Table 1. Essential parameters chosen for the structural design of the cells.

	BC truss	O truss	BC-O truss
Diagonal length (L)	0.707mm	0.707mm	0.707mm
Strut section (b/a)	0.5;1;2	0.5;1;2	0.5;1;2
Struts angle (θ)	90°	45°	45°

Polylactic Acid (PLA) was chosen as reference material because it exhibits shape memory behaviour and for its simplicity of manufacturing. The structures have been analysed with two different materials (material 1 and material 0) expressed through the ratio of Young Modulus

$$\frac{E_0}{E_1} = 1{,}1000 \quad (1)$$

where E_1 was set as 3149MPa representing the material with higher effective compressive stiffness while E_0 was considered as a theoretical modulus characterizing the material with lower effective compressive stiffness equals to 3.149MPa both with Poisson's ratio equals to 0.35. During the reduction of Young Modulus the material was expected to overcome the glass transition temperature (Tg) at 57 °C enabling the PLA to pass through the elastic phase. Moreover, it has been introduced the thermal expansion coefficient $\alpha=185*10^{-6}$ $°C^{-1}$ (Cesarano et al. 2021). The material's properties are listed in the table 2 below:

Table 2. PLA properties associated with the models and set on the software ABAQUS.

	MATERIAL 1	MATERIAL 0
Young Modulus [MPa]	3149	3.149
Poisson's ratio	0.35	0.35
Tg [°C]	57	57
α $[°C]^{-1}$	$185*10^{-6}$	$185*10^{-6}$

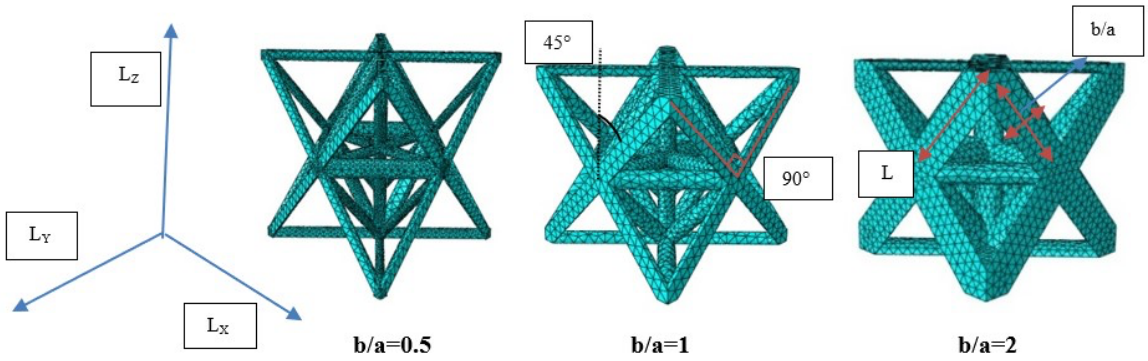

Fig. 1: Finite element mesh of the BC-O lattice unit cell.

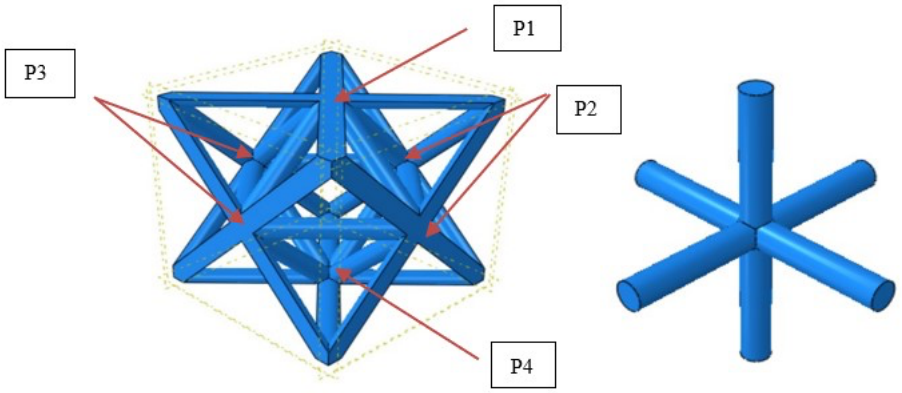

Fig. 2: schematic representation of the union between the BC and the O lattice unit cell.

As the relative density strongly influence the material's mechanical properties, as effective compressive stiffness and energy absorption, it represents a fundamental parameter for this research as it defines the thickness of the struts. It was calculated as the ratio between the volume of the beam and the total volume of the cell, **a** and **b** are the geometrical parameter of the ellipse and Lc is the length of the cubic size. The parameters follow the formulas below:

$$\rho = \frac{\sum V_{beam}}{V_{tot}}; \quad (2)$$

$$V_{beam} = \pi abL; \quad (3)$$

$$V_{tot} = Lc^3 \quad (4)$$

The effective stiffness $\bar{E}$ was calculated following the equation 5 as the ratio between the variation of stress and variation of strain, while the strain energy density, denoted by the symbol uppercase letter 'U', it is defined as the integral between 0 and ε of stress with the variable dε. The parameter U follows a computational formula described as the sum of each curves' stress multiplied by the difference of strain (equation 6):

$$\bar{E} = \frac{\Delta\sigma}{\Delta\varepsilon} = \frac{\sigma_{i+1}-\sigma_i}{\varepsilon_{i+1}-\varepsilon_i} \quad (5)$$

$$U/\sum V_{beams} = \sum_{i=1}^{n-1} \frac{\sigma_{i+1}-\sigma_i}{2} * (\varepsilon_{i+1} - \varepsilon_i) + \sum_{i=1}^{n-1} \sigma_i * (\varepsilon_{i+1} - \varepsilon_i) \quad (6)$$

where σ_{i+1} is the stress of the i+1 point of the curve while σ_i is the stress of the i point of the curve, ε_{i+1} is the strain of the i+1 point of the curve and finally, ε_i is the strain of the i point of the curve

Figure 3 outlines the complete study process proposed in this paper. Each structure was associated with the relative densities (0.15; 0.30; 0.60) related to the strut shape (0.5; 1; 2) aiming to reach the combination between the cells BC+O and between the material Mat_1+Mat_0

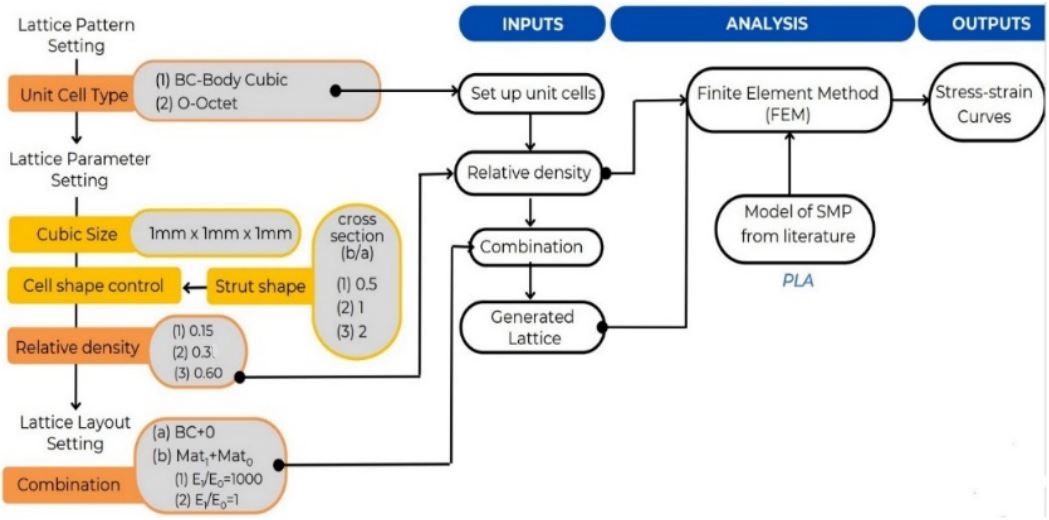

Fig. 3. Outline of the experimental and analysis process.

3. Finite Element Implementation

In this section the implementation of the model in the software ABAQUS is showed. The Static Analysis was used as the solver using the nonlinear geometry could have an effect on the results due to the high non-linearity of the model. As first step the buckling analysis was set to measure the instability of the model calculating the first eigenvalue of the stiffness matrix while, as second step, the post-buckling analysis was conducted to find the stress-strain curves as output. To simulate the uniaxial compression of the BC-O model, the top and bottom surfaces were coupled to constrain the movement to a single reference point (RP) which was placed in the central nodes respecting the coordinates (0,0,0) and (1,1,1) of the structure. The boundary conditions applied were an interlocking to keep blocked the lower surface while allowing a displacement of 1mm (in the negative Y direction) on the top surface so that the compression could be simulated. Then to reduce the degree of freedom a constrain along the X direction equal to 0 was set on the top surface. The quadratic tetrahedral mesh (C3D10) with distortion control was used.

4. Results and discussions

The mechanical behavior of the BC-O with various geometries and uniaxial compression load was evaluated using the 3D finite element simulations. In section 4.1, the shape memory results of the BC-O with relative densities, as showed in the Table 3, are described through the stress-strain curve obtained to the post-buckling analysis where each chart in Figures 4 and 5 represent the mechanical properties of the structure designed with different cross sections (Table 3), and different combinations of material as (table 4). Finally, the strain energy and effective stiffness are discussed in section 4.2 to measure the BC-O energy absorption and to evaluate the force-recovery and shape-recovery in terms of degradation of the structure.

Table 3: cross section of the BC-O truss associated with their relative densities

Cross section	Relative Densities
b/a= 0.5	ρ=0.15
b/a=1	ρ=0.30
b/a= 2	ρ=0.60

Table 4: combination of material 1 and material 0 with different stiffness ratios.

	MATERIAL 1	MATERIAL 0
MATERIAL 1	E1/E0= 1	$E1/E0=10^3$
MATERIAL 0	$E1/E0=10^{-3}$	E1/E0=1

4.1 BC-O structure's results under uniaxial compression

The stress-strain curves obtained were evaluated through a minimum strain of ε=10% defining, as boundary condition, the displacement in the middle point of the top surface, as discussed in the section 3. The results show four structures which represent the four combinations of stiffness ratio for each cross section: O1/BC1 (black line in Figure 4), O1/BC0 (green line in Figure 4), O0/BC1 (red line in Figure 4), O0/BC0 (blue line in Figure 4) where the label 1 is referring to the rigid material and 0 to the soft material, as showed in the Table 2. The more rigid structures are represented in the left charts with the black and green curves while the red and blue curves are showed in the right charts to evaluate the difference of stiffness based on the combination of material. The simulations were conducted, as first step, on the circular section (b/a=1) studying the mechanical properties of the simplest and regular geometry. Then, changing the geometrical parameters as showed in Table 1, considering the elliptical section, the ultra-low density and the low-density BC-O truss are simulated instead. The charts in the Figure 4 represent in (a) and (b) the structures measured with cross section b/a=1; in (c) and (d) the thinner structure with b/a=0.5, and finally in (e) and (f) the thicker structures. As it is showed in the Fig. 4 (a) the curves describe the behavior of the stiffer structures as the O1/BC1,which exhibits the highest stiffness and critical strength, leading it to be the most stable and resistant model to deformation capable to withstand significant loads without premature buckling, The curve rises steeply reaching a maximum stress (σ_{max}) of 4.43417MPa when the strain is ε=6% before gradually declining. Moreover, the O1/BC0 structure (green line) benefits from the stiffer octet (O) truss, which provides significant load-bearing capacity, and from the flexible BC truss which makes the structure more subjected to deformation, in fact, the maximum stress is lower than the O1/BC1 as it is σ_c=4.35174 MPa. In (b) are reported the softer structures O0/BC1 (red curve) and O0/BC0 (blue curve) where the first shifts the structural integrity toward the BC component, limiting the overall stiffness making it more prone to buckling due to the softer octet truss, while the second (blue line) represents the most flexible structure with the weakest performance in terms of structural stability and load-bearing capacity. Their critical strength is reached respectively at σ_c=0.004739 MPa and σ_c=0.00443418MPa. The thinner geometries (i.e., b/a=0.5) compromise the structures' stability to withstand compressive forces, leading to buckling under relative lower strain as showed in the figure 4 (c) and (d). In such a case the σ_{max} reached from these structures is σ_c=1.45147MPa for O1/BC1 (black curve) and σ_c=1.22843MPa for O1/BC0 (green curve) at circa ε=4%, while σ_c=0,0076316 MPa for O0/BC1 (red curve) and σ_c=0.0014514 MPa for O0/BC0 (blue curve). This geometry, while allowing for weight savings, weakens the configuration because the struts are slender enough to collapse during the first deformation, despite such flexibility could be advantageous in terms of energy absorption. In contrast, the thicker structures (i.e., b/a=2) showed in (e) and (f) exhibit the highest stiffness and stress capacity rather than the other typologies. As the σ_{max} reaches the highest values (σ_c=13,167MPa for O1/BC1 (black line) and σ_c=6.15391MPa for O1/BC0 (green line) at ε=9% while σ_c=0.0466146 for O0/BC1 (red line) and σ_c=0.013174MPa for O0/BC0 (blue

line)). In such scenario, the structures have more difficult in buckling due to the robustness of their struts offering in such a way superior critical strength supporting greater loads before failure.

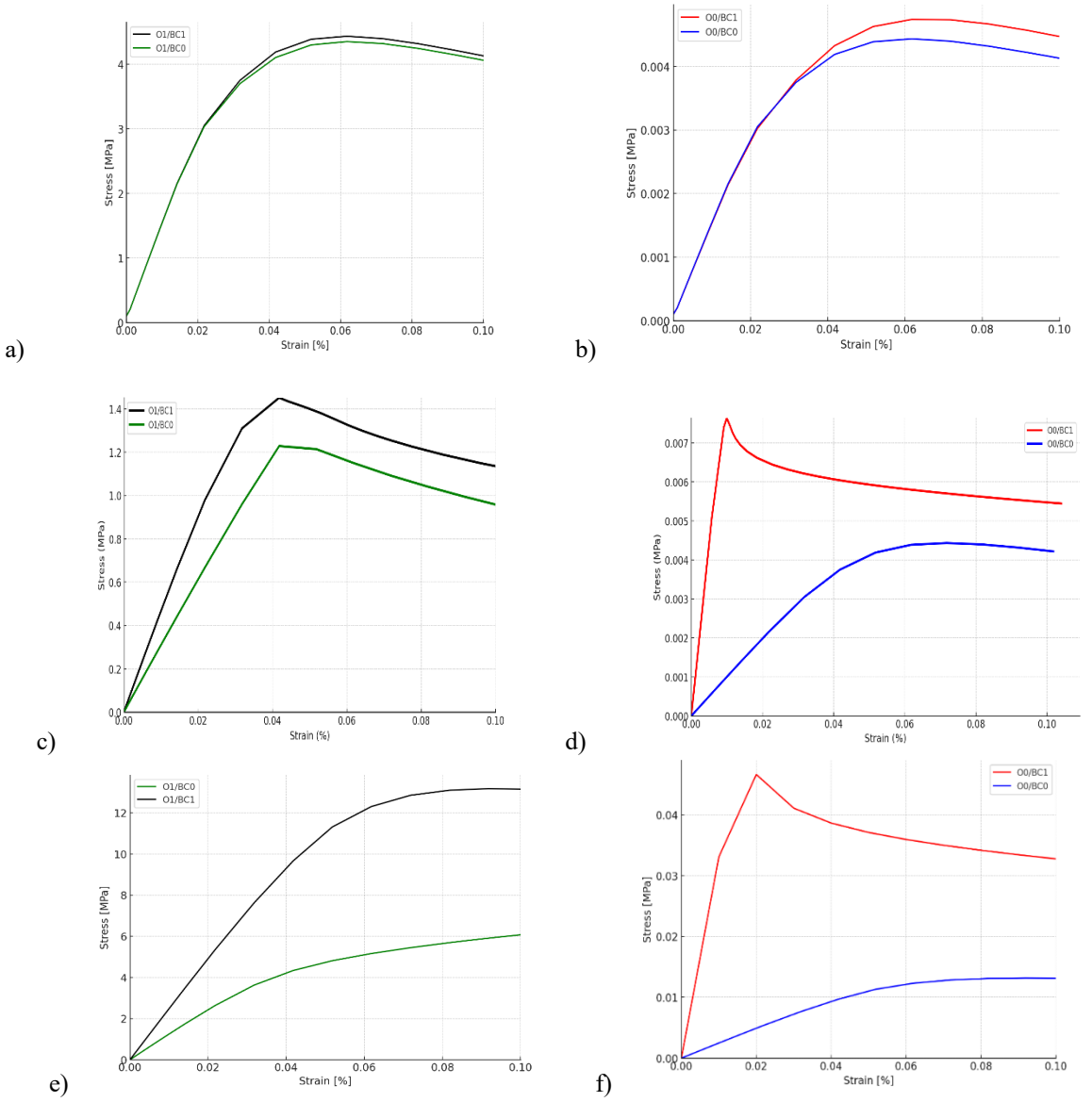

Fig. 4. Stress-Strain curves for the structures O1/BC1 (black), O1/BC0 (green), O0/BC1 (red) and O0/BC0 (blue) in the case of (a) (b) b/a=1, (c) (d) b/a=0.5 and (e)(f) b/a=2.

The diagrams showed in the Figure 5 compare (O-BC) structures at different relative densities. At ρ=0.15 (dotted lines) the structures are particularly flexible showing the lowest critical stress, meaning that they reach failure under lower loads, in particular the O0/BC0 in Fig.5 (d, blue dotted curve), making this structure ideal for energy absorption in low-load applications, but unsuitable for supporting higher mechanical stresses. Instead, the structure characterized by ρ=0.60 (dashed lines) are the most robust structures. In fact, they reach their peaks of stresses later than the others due to the little tendency of the struts to bend under loading. In addition, the linear behavior of the stress-strain curve is steeper and higher. Then, looking at the behavior of the circular structure represented through b/a=1 (full lines), a good compromise between the flexibility of the slender structure and the high stiffness of the thicker beams, is achieved. In this regard, these stress-strain curves reach the convergence easier than in other scenarios. Then, from the analysis of figure 5, is visible as with the increasing the relative density (from dotted to dashed lines), the O-BC structure shows a higher resistance to external load, while, decreasing the cross section (from dashed to dotted lines), the samples tends to bend more.

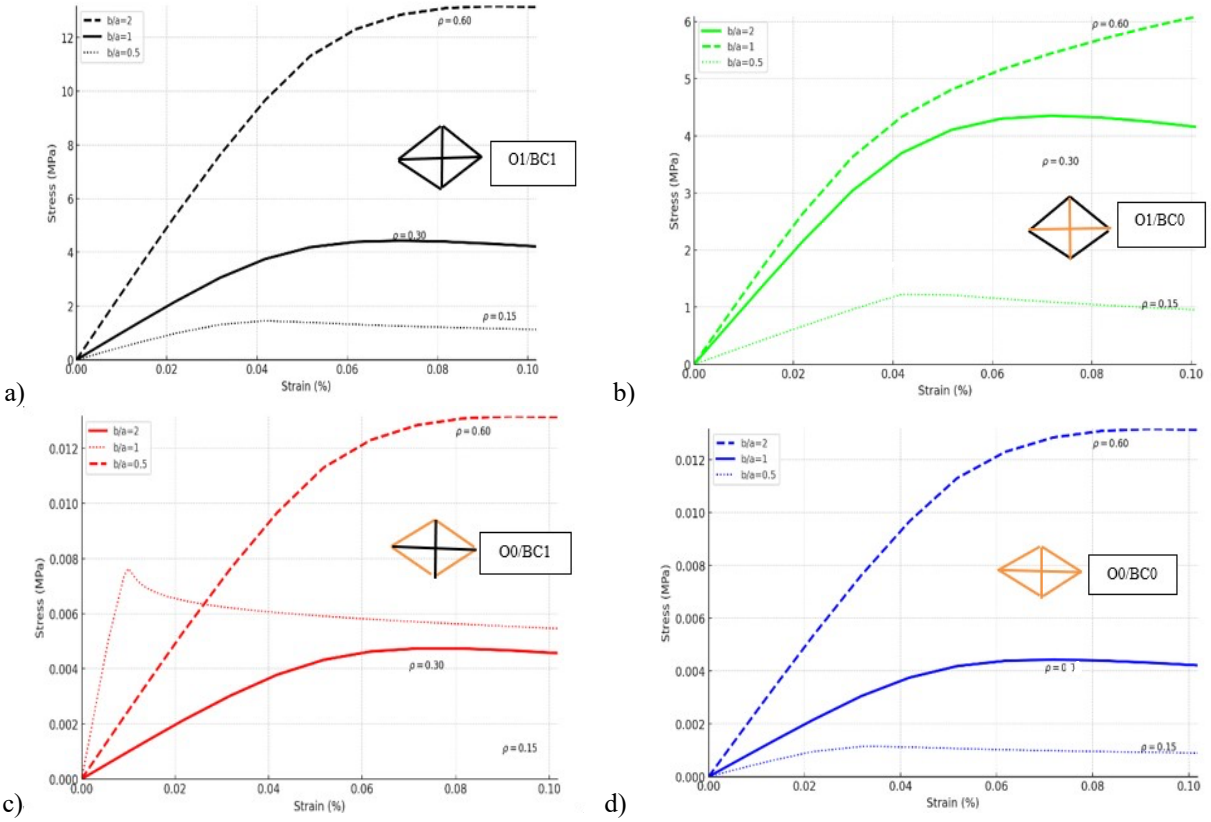

Fig. 5. Stress-Strain curves with associated relative densities (0.15-dotted line; 0.30-full line; 0.60- dashed line) in (a) O1/BC1 (black), (b) O1/BC0 (green), (c) O0/BC1 (red) and (d) O0/BC0 (blue).

4.2 Effective stiffness and strain energy

Geometrical parameters profoundly influence mechanical performance of the structures such as effective stiffness, critical strength and energy absorption. The effective stiffness $\bar{E}$ refers to the overall ability of a structure or material to resist deformation under compressive loads represented through the diagrams in the Figure 6 (a) and (b) depending on the variation of the cross section, while the strain energy is the potential energy absorbed by the body due to the deformation or strain effect showed in the diagram in the Figure 7 (a) and (b). Accordingly, to the results showed in the paragraph 4.1, the highest effective stiffness corresponds to the thicker structure (i.e., b/a=2) as the maximum is

reached by the O1/BC1 structure at $\bar{E}$ =1.28MPa (Figure 5, blue dot). This is confirmed to be the more robust structure due both to the combination of the stiffer material E1 and to the thickness of the beam. The combined structure presents an intermediate stiffness, in particular the O1/BC0 (red dots) represented on the diagram in the Figure 5 (a) is a little bit lower than the O1/BC1 due to the soft material associated with BC0. Looking at O0/BC1 (blue dot in Figure 5b), the effective stiffness is a little bit higher than the O0/BC0 due to the contribution of the stiffer material associated with BC1 as it is showed in the figure 5 (b). In this regard, the thinner O0/BC0 has the lowest effective stiffness $\bar{E}$ =0.00044 MPa at b/a=0.5 demonstrating that this is the less performative scenario as it is the most lightweighted and flexible.

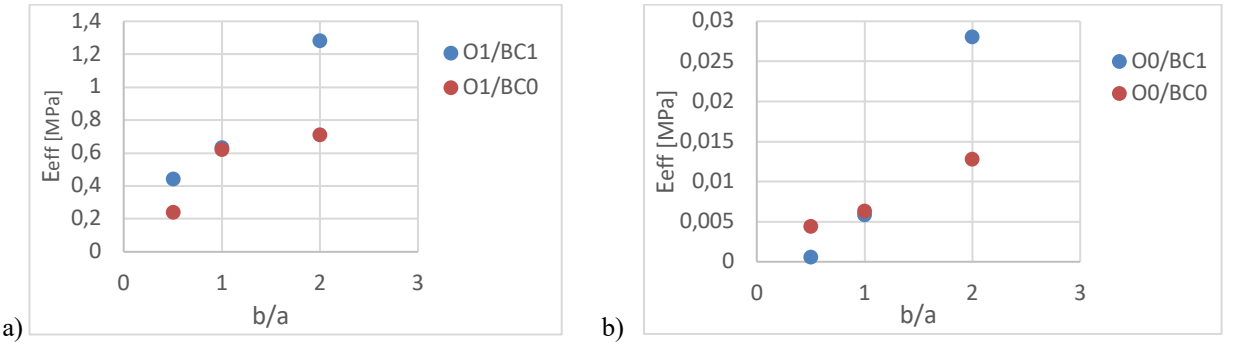

Fig. 6.Effective stiffness of the structures related to the cross section b/a. (a) The most rigid structures where the material E1 predominates, (b) the softer structures where the material E0 predominates.

As the total strain energy E represents the subtended area under the stress-strain curve, accordingly, the thickest structures absorb the greater quantity of energy as they offer resistance to deformation , unlike the slender structures. This means that the geometries perform well under moderate loads absorbing energy effectively while still maintaining a good flexibility .

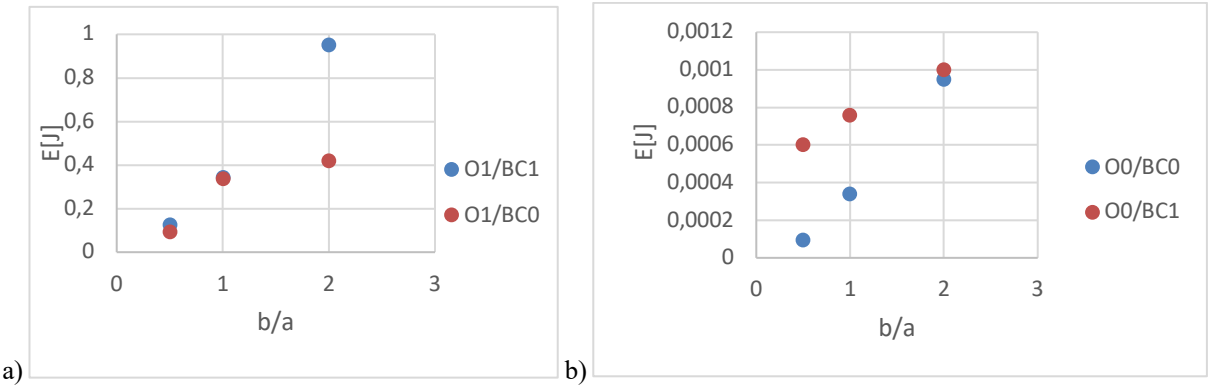

Fig. 7.Strain energy of the structures related to the cross section b/a. (a) The most rigid structures where the material E1 predominates, (b) the softer structures where the material E0 predominates.

Conclusions

In this preliminary study, we have investigated the mechanical performance as a function of stiffness ratio ($E1/E0 = 1{,}1000$) and topology (BC and O) under compression. Interestingly, the combination of Octet and body cubic by different stiffness ratio shows clearly different behaviours. When the stiffness of Octet structure is equal to 1000 times higher than that of body cubic structure, the effective stiffness and strength is much higher than the other combinations. Therefore, the combined structure is more sensitive to the material degradation when the material of

Octet has strong material degraded performance under external stimuli. Due to the computational cost, finite element simulation of one representative volume element (RVE) has been performed. Therefore, boundary conditions has strong effect on the mechanical behaviour and for this reason, we plan to investigate the behavior of multi-RVE to understand better the effect of such boundary conditions

References

Fan, Y., Miao, X., Hou, C., Wang, J., Lin, J., & Bian, F. (2023). High tensile performance of PLA fiber-reinforced PCL composite via a synergistic process of strain and crystallization. Polymer, 270, 125778 . https://doi.org/10.1016/j.polymer.2023.125778

Wang, K., Jia, Y.-G., Zhao, C., & Zhu, X. X. (2019). Multiple and two-way reversible shape memory polymers: Design strategies and applications. Progress in Materials Science, 105, 100572. https://doi.org/10.1016/j.pmatsci.2019.100572

Zhao, Q., Qi, H. J., & Xie, T. (2015). Recent progress in shape memory polymer: New behavior, enabling materials, and mechanistic understanding. Progress in Polymer Science, 49–50, 79–120. https://doi.org/10.1016/j.progpolymsci.2015.04.001

Eraslan, K., Altınbay, A., & Nofar, M. (2024). In-situ self-reinforcement of amorphous polylactide (PLA) through induced crystallites network and its highly ductile and toughened PLA/poly(butylene adipate-co-terephthalate) (PBAT) blends. International Journal of Biological Macromolecules, 272, 132936. https://doi.org/10.1016/j.ijbiomac.2024.132936

Cesarano, F., Maurizi, M., Gao, C., Berto, F., Penta, F., & Bertolin, C. (2022). Preliminary optimization of shape memory polymers geometric parameters to enhance the thermal loads' activation range. Procedia Structural Integrity, 42, 1282–1290. https://doi.org/10.1016/j.prostr.2022.12.163

Ling, C., Cernicchi, A., Gilchrist, M. D., & Cardiff, P. (2019). Mechanical behaviour of additively-manufactured polymeric octet-truss lattice structures under quasi-static and dynamic compressive loading. Materials and Design, 162, 106–118. https://doi.org/10.1016/j.matdes.2018.11.035

Huang, Y., Ren, H., Liu, Y., Xu, W., & Zhao, W. (2024). Bending shape memory properties and multi-scale viscoelastic behaviors of knitted-fabric reinforced polymer composites. Composites Science and Technology, 256, 110747. https://doi.org/10.1016/j.compscitech.2024.110747

Hussain, M., Khan, S. M., Shafiq, M., Al-Dossari, M., Alqsair, U. F., & Khan, S. U. (2024). Comparative study of PLA composites reinforced with graphene nanoplatelets, graphene oxides, and carbon nanotubes: Mechanical and degradation evaluation. Energy, 308, 132917. https://doi.org/10.1016/j.energy.2024.132917

Huang, L., Sheng, Y., Mo, Q., Zhang, S., Zheng, Y., Wang, B., Huang, C., Duan, Q., & Zhao, H. (2024). Poly(lactic acid)/polycaprolactone-based self-programmed photothermal responsive shape memory polymers. Reactive and Functional Polymers, 202, 105990. https://doi.org/10.1016/j.reactfunctpolym.2024.105990

Barletta, M., Gisario, A., & Mehrpouya, M. (2021). 4D printing of shape memory polylactic acid (PLA) components: Investigating the role of the operational parameters in fused deposition modelling (FDM). Journal of Manufacturing Processes, 61, 473–480. https://doi.org/10.1016/j.jmapro.2020.11.036

Tancogne-Dejean, T., & Mohr, D. (2018). Elastically-isotropic elementary cubic lattices composed of tailored hollow beams. Extreme Mechanics Letters, 22, 13–18. https://doi.org/10.1016/j.eml.2018.04.005

Park, K.-M., Min, K.-S., & Roh, Y.-S. (2022). Design optimization of lattice structures under compression: Study of unit cell types and cell arrangements. Materials, 15(1), 97. https://doi.org/10.3390/ma15010097

Slavković, V., Hanželič, B., Plešec, V., Milenković, S., & Harih, G. (2024). Thermo-mechanical behavior and strain rate sensitivity of 3D-printed polylactic acid (PLA) below glass transition temperature (Tg). Polymers, 16(1526), 1-17. https://doi.org/10.3390/polym16111526142

Roudbarian, N., Baniasadi, M., Nayyeri, P., Ansari, M., Hedayati, R., & Baghani, M. (2021). Enhancing shape memory properties of multi-layered and multi-material polymer composites in 4D printing. Smart Materials and Structures, 30(10), 105006. https://doi.org/10.1088/1361-665X/ac1b3b

Kozin, P., & Zubarev, I. (2022). Crystallinity effect on electron-induced molecular structure transformations in additive-free PLA. Polymer, 265, 125609. https://doi.org/10.1016/j.polymer.2022.

Xu, P., Lan, X., Zeng, C., Zhang, X., Zhao, H., & Leng, J. (2024). Compression behavior of 4D printed metamaterials with various Poisson's ratios. International Journal of Mechanical Sciences, 264, 108819. https://doi.org/10.1016/j.ijmecsci.2023.108819

Ahmad, M., Singh, D., Fu, Y. Q., Miraftab, M., & Luo, J. K. (2011). Stability and deterioration of a shape memory polymer fabric composite under thermomechanical stress. Polymer Degradation and Stability, 96(9), 1470-1477. https://doi.org/10.1016/j.polymdegradstab.2011.05.009

Tao, R., Xi, L., Wu, W., Li, Y., Liao, B., Liu, L., Leng, J., & Fang, D. (2020). 4D printed multistable metamaterials with mechanically tunable performance. Composite Structures, 252, 112663. https://doi.org/10.1016/j.compstruct.2020.112663

Wan, M., Yu, K., & Sun, H. (2022). 4D printed programmable auxetic metamaterials with shape memory effects. Composite Structures, 279, 114791. https://doi.org/10.1016/j.compstruct.2021.114791

Zhao, W., Yue, C., Liu, L., Leng, J., & Liu, Y. (2023). Mechanical behavior analyses of 4D printed metamaterials structures with excellent energy absorption ability. Composite Structures, 304, 116360. https://doi.org/10.1016/j.compstruct.2022.116360

Pirhaji, A., Jebellat, E., Roudbarian, N., Mohammadi, K., Movahhedy, M. R., & Asle Zaeem, M. (2022). Large deformation of shape-memory polymer-based lattice metamaterials. International Journal of Mechanical Sciences, 232, 107593. https://doi.org/10.1016/j.ijmecsci.2022.107593

Eraslan, K., Altınbay, A., & Nofar, M. (2024). In-situ self-reinforcement of amorphous polylactide (PLA) through induced crystallites network and its highly ductile and toughened PLA/poly(butylene adipate-co-terephthalate) (PBAT) blends. International Journal of Biological Macromolecules, 272, 132936. https://doi.org/10.1016/j.ijbiomac.2024.132936

Lumpe, T. S., & Shea, K. (2021). Computational design of 3D-printed active lattice structures for reversible shape morphing. Journal of Materials Research, 36(18), 3642–3655. https://doi.org/10.1557/s43578-021-00225-2

Dong, L., Jiang, C., Wang, J., & Wang, D. (2021). Design of shape reconfigurable, highly stretchable honeycomb lattice with tunable Poisson's ratio. Frontiers in Materials, 8, 660325. https://doi.org/10.3389/fmats.2021.660325

Gross, A., Pantidis, P., Bertoldi, K., & Gerasimidis, S. (2019). Correlation between topology and elastic properties of imperfect truss-lattice materials. Journal of the Mechanics and Physics of Solids, 124, 577–598. https://doi.org/10.1016/j.jmps.2018.11.007

Fan, P., Chen, W., Zhao, B., Hu, J., Gao, J., & Fang, G. (2018). Formulation and numerical implementation of tensile shape memory process of shape memory polymers. Polymer, 148, 370– 381. https://doi.org/10.1016/j.polymer.2018.06.054

Zheng, G., Zhang, L., Wang, E., Yao, R., Luo, Q., Li, Q., & Sun, G. (2022). Investigation into multiaxial mechanical behaviors of Kelvin and

Fuller RB. Octet Truss 1961;986:241. U.S. Patent No. 2.

Chen XY, Tan HF. An effective length model for octet lattice. Int J Mech Sci 2018; 140:279–87.

Al Azzawi, W., Epaarachchi, J. A., & Leng, J. (2018). Investigation of ultraviolet radiation effects on thermomechanical properties and shape memory behaviour of styrene-based shape memory polymers and its composite. Composites Science and Technology, 165, 266-273. https://doi.org/10.1016/j.compscitech.2018.07.001